

Contents lists available at ScienceDirect

Corrosion Science

journal homepage: www.elsevier.com/locate/corsci





High-throughput aqueous passivation behavior of thin-film vs. bulk multi-principal element alloys in sulfuric acid

William H. Blades ^{a,b}, Debashish Sur ^{c,d}, Howie Joress ^e, Brian DeCost ^e, Emily F. Holcombe ^{f,g}, Ben Redemann ^{f,h,i}, Tyrel M. McQueen ^{f,h,i}, Rohit Berlia ^a, Jagannathan Rajagopalan ^a, Mitra L. Taheri ^f, John R. Scully ^{c,d}, Karl Sieradzki ^{a,*}

- ^a Ira A. Fulton School of Engineering, Arizona State University, Tempe, AZ 85287, USA
- ^b Department of Physics and Engineering Physics, Juniata College, Huntingdon, PA 1665, USA
- ^c Center for Electrochemical Science and Engineering, University of Virginia, Charlottesville, VA 22904, USA
- ^d Department of Materials Science and Engineering, University of Virginia, Charlottesville, VA 22904, USA
- ^e Materials Measurement Science Division, National Institute of Standard and Technology, Gaithersburg, MD 20899, USA
- f Department of Materials Science and Engineering, Johns Hopkins University, Baltimore, MD 21218, USA
- ⁸ Naval Surface Warfare Center, Carderock, West Bethesda, MD, USA
- ^h Department of Chemistry, The Johns Hopkins University, Baltimore, MD 21218, USA
- ⁱ William H. Miller III Department of Physics and Astronomy, The Johns Hopkins University, Baltimore, MD 21218, USA

ARTICLE INFO

Keywords: Passivation Surface passivation Intergranular corrosion Acid corrosion Corrosion resistance

ABSTRACT

Multi-principal element alloys have the potential to show excellent passivation behavior. However, the detailed compositional and crystal structure design of these alloys requires a high-throughput strategy. We used combinatorial thin-film libraries of single-phase (FeCoNi) $_{1-x-y}$ Cr $_x$ Al $_y$ alloys and compared their passivation behaviors to corresponding bulk alloys. Our results demonstrate that the detailed passivation behaviors of thin-films and bulk alloys are different which is related to both nanoscale porosity within the thin-films and grain boundary dissolution. Nevertheless, we found that comparisons made among suitably designed sets of thin-film alloys can be used to determine the best corrosion performing bulk alloy composition.

1. Introduction

Multi-principal element alloys (MPEAs) have recently attracted significant attention due to their promising mechanical behavior [1–3], corrosion performance [4,5], and high temperature oxidation resistance [6]. While the emergence of these alloy classes initially focused on equiatomic systems with 4–5 components [3,7,8], MPEAs now occupy a much broader composition space with an emphasis on alloying equiatomic base MPEAs with off-equiatomic amounts of other elements. Such an approach allows for tuning alloy properties with the addition or removal of relatively dilute amounts of different elements. As it pertains to the study and design of corrosion-resistant alloys, the main emphasis has involved selectively alloying a base multi-component alloy with known passivating elements such as Cr, Al, Ti, and Si [4,9–15]. With such complex alloy compositions, the interplay between the passivating components and the overall electrochemical behavior of the alloy has yielded intricate aqueous passivation processes that are not yet fully

understood.

The effect of Cr and Al on the primary and complete passivation behaviors of binary alloys has been investigated in both sulfate and chloride environments [16-20]. Herein, primary passivation refers to the initial stage of the passivation process involving O2- incorporation into about top 1-3 monolayers of the alloy surface and occurring over time scales less than one second [16,21]. Complete passivation corresponds to the development of a thicker passive film of order a few nanometers which occurs over time scales of many minutes to hours. The effect of Al on binary Fe_{1-v} Al_v (throughout this manuscript, alloy subscripts refer to mole fractions) alloys is complex, where an increase in Al content was shown to have a minimal effect on the passivation behavior of the binary alloy until the concentration exceeded a mole fraction of about 0.20 [17,19,20]. While these results show that an increase in these components can improve passivation behavior, their addition in larger relative quantities does not guarantee a proportional increase in performance.

E-mail address: karl.sieradzki@asu.edu (K. Sieradzki).

 $^{^{\}ast}$ Corresponding author.

With regard to the effect of larger amounts of Cr in "Cantor-type" MPEAs (e.g., FeCoNi or MnFeCoNi), Chai and Pan examined the passivation behavior of the equiatomic ternary FeCoNi alloy with Cr additions of 0.143 and 0.25 mol fraction [22]. The (FeCoNi) $_{0.858}$ Cr $_{0.143}$ alloy exhibited superior performance in both sulfate and chloride electrolytes, while the equiatomic FeCoNiCr alloy did not perform as well due to the formation of a Cr-containing second phase. The presence of an electrochemically active element such as Mn can affect the efficiency of the primary passivation process [23]. Luo et al. compared the corrosion resistance of an equiatomic CoCrFeMnNi to that of 304L stainless steel [24]. They found 304L displayed superior passivation performance, and we suggest that this was likely a result of the high concentration of Mn in the equiatomic alloy.

Alloying Al in Cantor-type MPEAs leads to even more complex behaviors. Generally, Al concentrations larger than a mole fraction of about 0.08 results in the formation of secondary phases such as the NiAl B2 phase in the surrounding FCC matrix [25]. The impact of this microstructural change on corrosion performance has been measured directly by Yen et al. who electrochemically tested heat treated equiatomic AlCoCrFeNi alloys in a sulfate environment and found the B2 phase preferentially corroded, with respect to the surrounding FCC matrix [26]. This adverse effect was further exacerbated in chloride containing electrolytes, where increased Al concentrations in CoCrFeMnNi-Al alloys decreased the alloy's corrosion resistance and resulted in pitting. The unfavorable effect of Al additions on the corrosion performance of non-equiatomic Cr_{0.24}Fe _{0.38}Mn_{0.25}Ni _{0.13} alloys was further highlighted by Lee et al. who observed an increase in both the i_{crit} and i_{pass} , the critical current density and the passive current density respectively, with increasing Al concentration [27].

Previous research has explored how alloy thin-films can be electrochemically tested to unravel the effect of composition and crystal structure on corrosion behavior using high-throughput methodologies [28]. These methods have been used to evaluate a number of corrosion related issues including but not limited to, corrosion inhibitors [29,30], dielectric properties [31], anodization [32,33] and anisotropic dissolution [34]. Herein we focus on the use of these thin-films as a surrogate for screening bulk alloys. These approaches use gradient metallic thin-film alloys, produced by vacuum deposition processes such as evaporation or sputtering, which results in a compositional gradient across a substrate of order a few atomic percent per centimeter [32–34]. This method can be used to rapidly screen a large number of crystal structures and compositions for different behaviors relevant to corrosion.

In this manuscript, we used a high-throughput technique to examine whether MPEA thin-film aqueous passivation metrics can be used to down-select the crystal structures and compositions yielding the best passivation behavior of corresponding bulk alloys. We chose to explore the behavior of (FeCoNi)_{1-x-v}Cr_xAl_v alloys over a large composition space, using thin-film combinatorial library (CL) wafers with compositional gradients. Electrochemical measurements across two (FeCoNi)_{1-x-} _vCr_xAl_v combinatorial-library wafers, containing both single-phase and multi-phase regions, were made using a custom flowing scanning droplet cell (SDC) [35-37]. The SDC allowed us to electrochemically characterize selected 4 mm diameter "spots" on the 76 mm diameter combinatorial wafers. The electrolyte used in all of the experiments was 0.10 mol/L H₂SO₄. Electrochemical characterizations of selected spots occurred sequentially by first determining the impedance modulus, | $Z|_{\text{OCP}}$ of the air-formed film in the electrolyte, after which the film was cathodically reduced prior to the initiation of linear sweep voltammetry (LSV). The relative variations in passivation performance across the single-phase CL wafer regions were then directly compared against a set of corresponding induction-melted bulk $(FeCoNi)_{1-x-y}Cr_xAl_y$ (x =0.04-0.10, and y fixed at 0.03 or 0.06) alloys and a single composition, single-phase $(FeCoNi)_{0.84}Cr_{0.10}Al_{0.06}$ thin-film alloy following similar protocols. Significant differences in the passivation behaviors were observed among CL wafer spots, the bulk alloys and the single

composition thin-film alloy, as a result of the porosity and intergranular corrosion in the thin-film alloys. The microstructure of the (FeCo-Ni) $_{0.84}$ Cr $_{0.10}$ Al $_{0.06}$ alloy thin-film and its bulk counterpart was characterized to further explore the morphological variations between formats. The composition of the grain interiors and grain boundaries in the single composition (FeCoNi) $_{0.84}$ Cr $_{0.10}$ Al $_{0.06}$ thin-film was characterized with STEM-EDS.

2. Methods

2.1. Combinatorial library wafer deposition

Two continuous gradient (FeCoNi) $_{1\text{-}x\text{-}y}\text{Cr}_x\text{Al}_y$ thin-film combinatorial libraries (CL) wafers were synthesized by co-sputtering from three non-coincident magnetron sources onto 76 mm Si wafers with a thermally grown SiO $_2$ layer. The alloys were sputtered from a set of metallic targets: Cr, Al, and Fe $_{0.33}\text{Co}_{0.33}\text{Ni}_{0.33}$, each with purities of better than 99.9 %. Cr was sputtered at 23 W/cm 2 RF and Al at 14 W/cm 2 DC. The DC sputtering power for the alloy target was altered between the two library wafers at 58 W/cm 2 and 92 W/cm 2 , respectively. Before deposition, the base pressure of the chamber was 4.5 μPa . During deposition, the chamber was filled with Ar (> 99.99 % purity), such that the chamber pressure had a background of approximately 930 mPa. After deposition, the wafers were annealed under vacuum at 600 °C for 8 h. Supplementary Table S1 lists the crystal structures and compositions of selected wafer spots.

2.2. Bulk (FeCoNi)-Cr-Al alloy preparation

A set of bulk (FeCoNi)_{1-x-y}Cr_xAl_y samples, x, and y are in mole fractions (x = 0.04–0.10, y = 0.03–0.06), were prepared by arc melting using pure elements: 99.95 % Fe, 99.95 % Co, 99.995 % Ni, 99.99 % Al and 99.95 % Cr (Kurt J. Lesker Company). To make a direct comparison to the thin-film samples, an additional bulk (FeCoNi)_{0.84}Cr_{0.10}Al_{0.06} alloy sample, using high purity metals (> 99.95 %, Neyco), was prepared by induction melting in a water-cooled copper crucible under a He atmosphere with a 50 kW power source at a frequency of 150 kHz. All ascast samples were then encapsulated in quartz tubes with a forming gas (95 % Ar + 5 % H₂) and Ta foil getter. Each alloy button was then homogenized at 1000 °C for 48 h and quenched into an ice water bath, where the quenching process was expedited by smashing the quartz tube. Before electrochemical characterization, each bulk alloy surface was polished with a diamond suspensions to a 1 μ m finish. Table S1 lists the crystal structure and composition of these bulk alloys.

2.3. Single-composition thin-film preparation

A non-combinatorial single-composition (FeCoNi) $_{1\text{-x-y}}\text{Cr}_x\text{Al}_y$ thinfilm was sputter deposited on a 200 µm thick, 100 mm diameter Si (001) wafer using an AJA Orion 5 sputtering system, yielding a 750 nm thick film. Ni (purity 99.995 %.), Fe (purity 99.95 %), and Co (purity 99.95 %) were deposited at 2.51 W/cm², 4.04 W/cm², and 3.35 W/cm², respectively, using DC power supplies whereas Al (purity 99.999 %) and Cr (purity 99.95 %) were deposited at 2.46 W/cm² and 2.66 W/cm², respectively, using RF power supplies. The deposition rates were determined using a crystal thickness monitor. The deposition rate of Ni, Fe, Cr, Al, and Co was 2.9 nm/min, 3 nm/min, 1.4 nm/min, 1 nm/min, and 2.9 nm/min, respectively. The base pressure of the chamber before deposition was less than 6.6×10^{-6} Pa. The deposition was performed at

[†] Certain equipment, instruments, software, or materials are identified in this paper in order to specify the experimental procedure adequately. Such identification is not intended to imply recommendation or endorsement of any product or service, nor is it intended to imply that the materials or equipment identified are necessarily the best available for the purpose.

0.4 Pa Ar pressure and the substrate was rotated during deposition at 40 rpm to achieve uniformity in film thickness across the substrate. Table S1 lists the crystal structure and composition of the thin-film.

2.4. X-ray diffraction analysis of alloy samples

The crystal structure of the CL wafers was measured using X-ray diffraction at the Stanford Synchrotron Radiation Light Source beamline 1–5. Diffraction patterns of 177 alloy spots on each CL wafter were collected using a fixed near-grazing incidence angle and an area detector. After measurement, the diffraction data were analyzed using CombiView and reference structures from the Materials Project database [37] A peer review classification process as described by Hattrick-Simpers et al. [38] was followed and is discussed in greater detail in [39].

Diffraction data on the bulk and single-composition thin-film alloys were collected on a Malvern PANalytical Empyrean diffractometer as shown in Supplementary material Fig. S1. Diffraction was measured using Cu K α radiation with a source excitation voltage of 45 kV and a current of 40 mA and scans were performed with a scan rate of 3°/min over a 2θ scanning range of 20–120°. An area scan was used for these samples to reduce the effects that texture may have had on peak intensity ratios. Due to the presence of Fe and Co, which fluoresce under Cu radiation, the proportional height detection levels of the detector were adjusted to have a range of 50–75 % to reduce the background radiation and better uncover diffracted intensity peaks. The diffraction data shown in Fig. S1 were stripped of K α 2 peaks, in post-processing.

2.5. Compositional analysis of alloy samples

The composition of each spot on the combinatorial wafer was measured using x-ray fluorescence (XRF) across a grid of 177 spots using a Bruker M4 Tornado, and analyzed by Crossroads XRS-MTFFP software using a standards-based thin-film analysis. The compositions of both the bulk and single-composition thin-film alloy samples were confirmed using a Helios UC G4 SEM equipped with energy-dispersive spectroscopy (EDS) and analyzed using the AzTec software. The compositions of these samples are provided in Table S1. The compositional variation across a single alloy spot was less than 2 at%.

2.6. Grain structure measurements of thin-film and bulk samples

As shown in Fig. S2, the grain structure and grain size distribution of the non-combinatorial single composition (FeCoNi) $_{0.84}$ Cr $_{0.10}$ Al $_{0.06}$ thinfilm sample was characterized using scanning transmission electron microscopy (STEM). Lift outs of the sample were prepared with a Helios UC G4 focused ion beam system using a field emission electron source. STEM micrographs and elemental distribution maps were acquired from these lift outs with EDS, in cross section, using a probe-corrected Thermo Fisher Scientific Themis Z STEM operating at 200 kV. A Super X EDX system is used in combination with a high-angle annular dark field detector for imaging. The grain structure of the bulk (FeCo-Ni)_{0.84}Cr_{0.10}Al_{0.06} sample was measured using a Quanta 650 scanning electron microscope (SEM) using a circular backscatter (CBS) detector. Before imaging, the bulk sample was polished to a 1 µm finish and then ion-polished for 12 minutes to provide high contrast between individual grains. ImageJ was used to measure the grain sizes on both the thin-film and bulk samples, as shown in Supplementary Figs. S3 and S4.

2.7. Microstructural analyses of CL thin-films

SEM analysis of corroded and uncorroded CL thin-film surfaces was performed using a Thermo Fisher Scientific Helios UC G4 scanning electron microscope SEM in the secondary electron mode using a $20~\rm kV$ accelerating voltage, beam current of $3.2~\rm nA$, and a dwell time of $1~\rm \mu s$.

2.8. Aqueous passivation behavior of thin-film and bulk samples

The (FeCoNi) $_{1\text{-}x\text{-}y}\text{Cr}_x\text{Al}_y$ CL wafers were electrochemically characterized using a modified Ametek scanning droplet cell (SDC) described in Joress et al. [37]. It consisted of a commercial saturated Ag/AgCl reference electrode (E = + 197 mV vs. SHE, standard hydrogen electrode), and Pt wire counter electrode in a deaerated (high purity N $_2$ gas) 0.10 mol/L $_2\text{SO}_4$ electrolyte. The bulk alloys and single-composition thin-films were characterized using a conventional flat three-electrode electrochemical cell comprised of a mercury/mercurous sulfate reference electrode (E = +640 mV vs. SHE), a Pt mesh counter electrode, and the bulk or thin-film alloy samples as working electrodes. A Gamry Interface 1000 potentiostat was used.

The same electrochemical protocol was followed for all samples as described here. The open circuit potential (OCP) was measured for 1800 s, followed by electrochemical impedance spectroscopy (EIS) at OCP using a 20 mV (RMS) amplitude AC signal from 100 kHz to 10 mHz recording 5 points per decade change in frequency. Subsequently, the native air-formed oxide was cathodically reduced by applying a series of potentials (vs. SHE): (i) -0.76 V for 300 s, (ii) -1.26 V for 3 s, (iii) -0.76 V for 60 s, and (iv) -0.36 V for 10 s, while using N_2 gas to remove any bubbles from the surface of the sample surface. After an OCP measurement for 10 s, LSV was performed from -0.1 V vs. OCP to 1.0 V at a scan rate of 5 mV/s. For comparing the alloy re-passivated film impedance at +600 mV, the single composition thin-film and bulk alloy surfaces were cathodically reduced to remove the air-formed film following the reduction protocol described above. The surface was then potentiostatically held at + 600 mV for 1800s to perform an EIS measurement using a 20 mV (RMS) AC signal from 100 kHz to 10 mHz recording 5 points per decade change in frequency. During the 1800 s potentiostatic hold, an AC signal of amplitude 20 mV (RMS) and frequency of 5 Hz, was used to characterize the film formation and growth behavior using chronoamperometry and imaginary impedance, Zimag. Based on our experience, we estimate the uncertainty (2 standard deviations) to be $\pm\,10\,\mu\text{A/cm}^2$ for i_{pass} and $i_{\text{crit}}.$ For $|Z|_{\text{OCP}}$ we estimate it to be $\pm 10 \ \Omega \cdot \text{cm}$ and $\pm 100 \ \Omega \cdot \text{cm}^2$ for values smaller and larger than 1000 $\Omega \cdot \text{cm}^2$, respectively.

3. Results

Prior to electrochemical measurements, as shown in Fig. 1, each region of the $\,$

 $(\text{FeCoNi})_{1\cdot x\cdot y}\text{Cr}_x\text{Al}_y$ combinatorial library (CL) wafers (x and y are in mole fraction) was characterized by both their composition and crystal structure using XRF and synchrotron XRD. Figs. 1A and 1B show a map of the individual spots on the wafers (177 on each wafer) that were identified by their respective crystal structures, labeled as FCC (F), FCC + BCC (FB), and FCC + BCC + B2 (FBB2) (see Table S1). The gradient composition of both wafers led to a wide compositional range. As shown in Fig. 1C, all data points were plotted on a partial pseudo-ternary phase diagram. The Cr_x and Al_y content in the CL wafers varied over the approximate range of x=0.05-0.20 and y=0.05-0.30, while the Fe, Co, and Ni compositions were roughly equimolar, with each species having a mole fraction of 0.20–0.30.

Once the structural and compositional analysis of the CL wafers was determined, aqueous electrochemical measurements were made using a SDC following the sequence outlined in the Methods section above. Fifty SDC measurements were made across the two wafers, and we analyzed 20 of these spots in detail. These particular spots were chosen since they had compositions close to that of the bulk alloys that we examined. The LSV and EIS data are plotted on a pseudo-ternary phase diagrams in Fig. 2 to highlight the differences in the electrochemical passivation for both single-phase and multi-phase alloy wafer spots. Measured $|Z|_{\rm OCP}$ values of the aged electrolyte exposed air-formed film are shown in Fig. 2A, which ranged from about 0.8 k $\Omega\cdot{\rm cm}^2$ to 150 k $\Omega\cdot{\rm cm}^2$. After the EIS measurement at OCP, the air-formed film was cathodically reduced

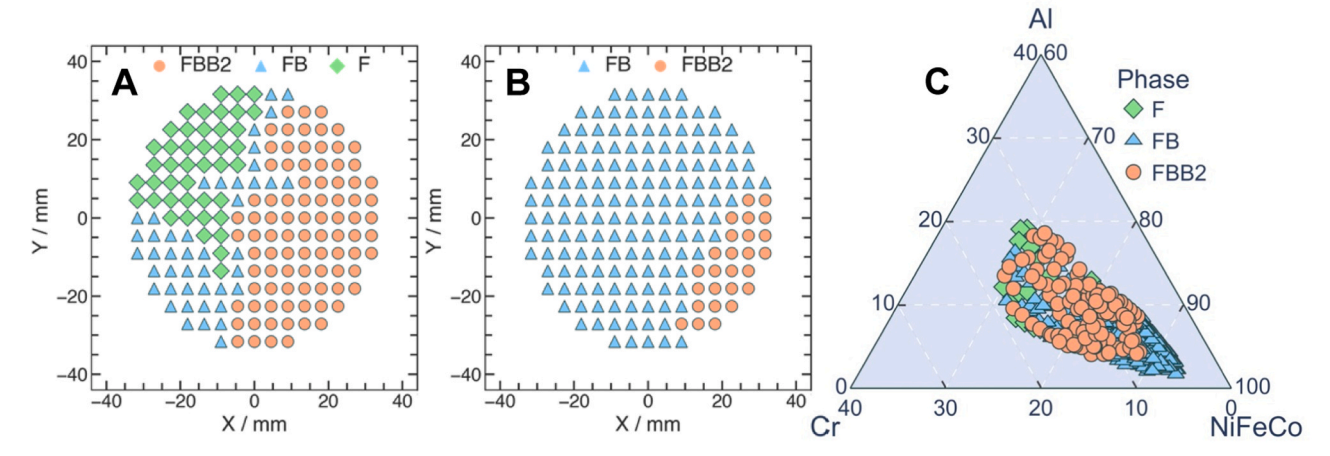


Fig. 1. Compositions and crystal structures of the combinatorial library wafers. XRD at each spot on the wafer was measured and is displayed as coordinate maps in (A) and (B). These spots are plotted on a pseudo-ternary phase diagram in (C) as a function of composition. The FCC, FCC + BCC, and FCC + BCC + B2 (see Table S1) are represented by green diamonds, blue triangles, and orange circles, respectively.

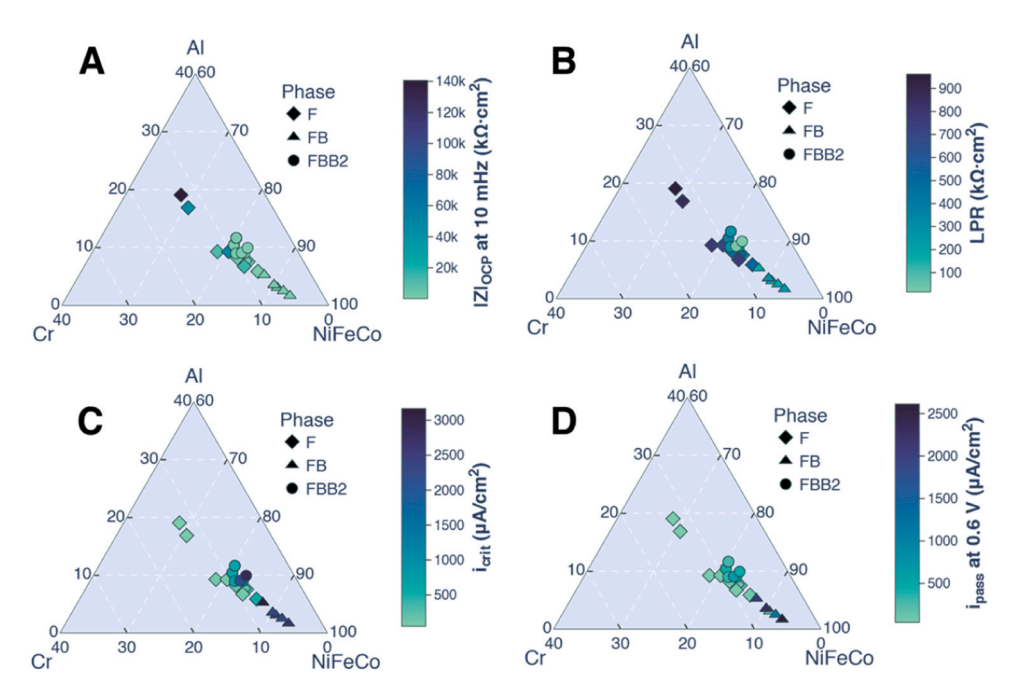


Fig. 2. Scanning droplet cell results on CL wafers. EIS measurements at OCP were taken prior to reduction of the air-formed film. (A) $|Z|_{OCP}$ of the impedance at 0.01 Hz. (B) After the reduction of the air-formed oxide, LPR was measured. (C) LSV determination of the critical current density for passivation, i_{crit} and (D) passive current density, i_{pass} , at + 0.6 V vs. SHE.

and LSV was measured across the (FeCoNi)_{1-x-y}Cr_xAl_y wafer alloy surface. These measurements were also used to determine using linear polarization resistance (LPR) measurements as shown in Fig. 2B [40]. The critical current density for passivation, i_{crit} , and the passive current density, i_{pass} , obtained from LSV are plotted in Figs. 2C and 2D and were found to vary from $100~\mu\text{A/cm}^2$ to $3200~\mu\text{A/cm}^2$ and $100~\mu\text{A/cm}^2$ to $2600~\mu\text{A/cm}^2$, respectively, depending on alloy composition. The EIS data revealed two general trends: first, the impedance modulus of the air formed film increases with the Cr + Al content in the alloy and second, the single-phase alloy regions have higher relative impedance values than the multi-phase alloy regions.

The voltammetry data (LPR, i_{crit} and i_{pass}) show similar trends, with a maximum in polarization resistance and a minimum in the critical current densities for single phase regions with higher Cr + Al compositions. Electrochemical LPR, as well as i_{crit} and i_{pass} parameters of all individual spots tested are plotted with respect to $|Z|_{OCP}$ as shown in

Fig. 3. The plot highlights the trend that $|Z|_{\rm OCP}$ correlates with a lower i_{crit}, i_{pass} and higher LPR values, which is in good agreement with our previous results [39], and provides further insight that relative trends in $|Z|_{\rm OCP}$ across single-phase and multi-phase regions are valuable as a high-throughput approach for identifying the composition(s) showing the best passivation behavior.

Fig. 4A presents the SDC LSV characterizations of (FeCoNi) $_{1\text{-}x\text{-}y}\text{Cr}_x\text{Al}_y$ CL alloy wafer spots. For these spots, the (FeCoNi) content was roughly equiatomic and the Cr and Al contents ranged between x=0.08-0.17 and y=0.06-0.19. These data show that an increase in the Cr + Al content generally resulted in a decreased i_{crit} from $600~\mu\text{A/cm}^2$ to $50~\mu\text{A/cm}^2$ and a lower i_{pass} ranging from $150~\mu\text{A/cm}^2$ to $40~\mu\text{A/cm}^2$. In order to understand differences in passivation performance between the CL wafers and bulk alloys, Fig. 4B compares the single composition (FeCoNi) $_{0.84}\text{Cr}_{0.10}\text{Al}_{0.06}$ thin-film (dashed-red line) LSV data to the set of induction-melted bulk (FeCoNi) $_{1\text{-}x\text{-}y}\text{Cr}_x\text{Al}_y$ alloys, where the Cr content

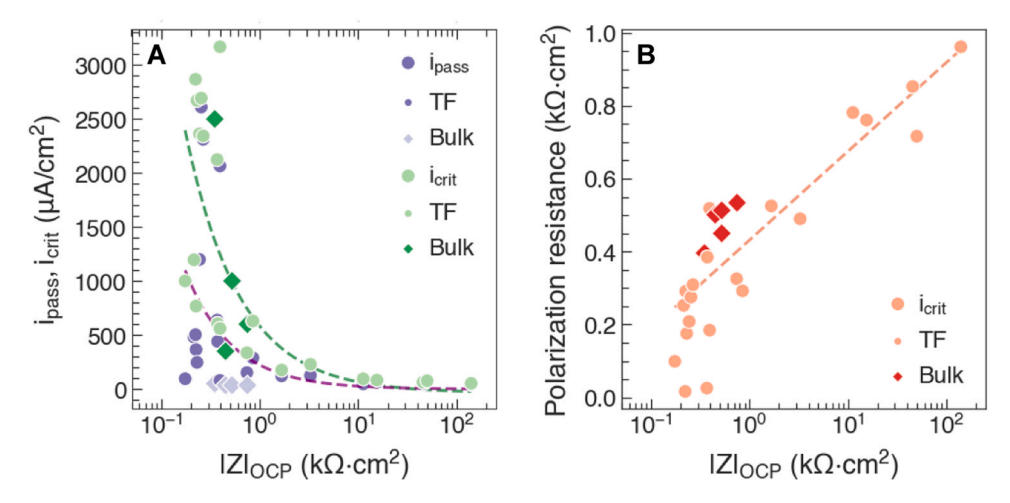


Fig. 3. Electrochemical passivation metrics. (A) i_{crit} and i_{pass} vs. $|Z|_{OCP}$ (B) linear polarization resistance (LPR) after cathodic reduction of air-formed oxide.

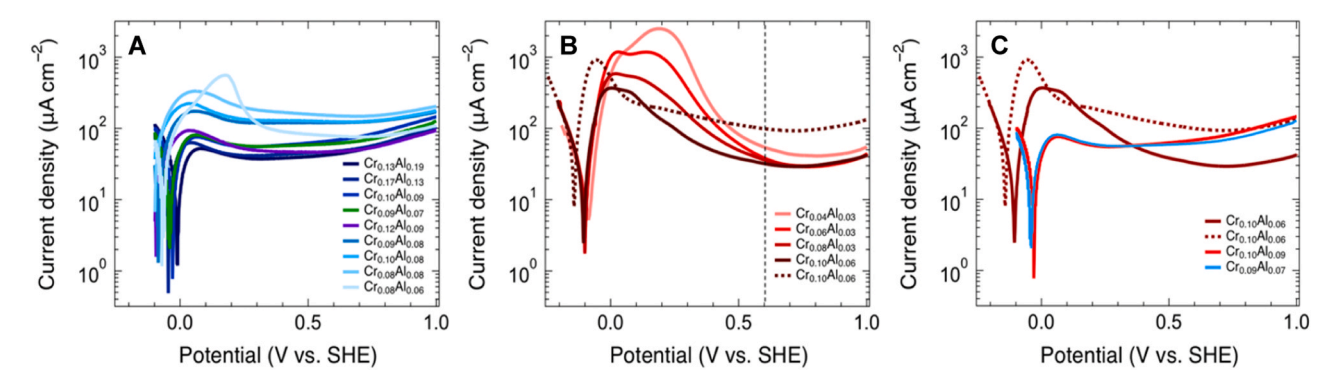


Fig. 4. LSV in 0.10 mol/L H_2SO_4 at 5 mV/s. (A) the CL wafer at the indicated (FeCoNi) $_{1.x.y}$ Cr_xAl_y compositions. (B) bulk (FeCoNi) $_{1.x.y}$ Cr_xAl_y (solid red lines) and single composition (FeCoNi) $_{0.84}$ Cr $_{0.10}$ Al $_{0.06}$ thin-film (dashed-red line). The curves in (B) are averaged from three experimental runs. All compositions marked on the figures are in mole fractions. The thin-dashed vertical black line at 600 mV indicates the voltage step applied during EIS (Fig. 5).(C) Comparisons of the bulk (FeCoNi) $_{0.84}$ Cr $_{0.10}$ Al $_{0.06}$ alloy, single composition (FeCoNi) $_{0.84}$ Cr $_{0.10}$ Al $_{0.06}$ thin-film alloy and CL wafer spots at the compositions of Fe $_{0.244}$ Co $_{0.295}$ Ni $_{0.264}$ Cr $_{0.104}$ Al $_{0.093}$ and Fe $_{0.254}$ Co $_{0.309}$ Ni $_{0.273}$ Cr $_{0.087}$ Al $_{0.077}$.

varied from x = 0.04 to 0.10 and the Al content was fixed at y = 0.03 or y = 0.06. This shows that the thin-film displays a corrosion potential that is shifted by about - 50 mV with that of the bulk alloys suggesting a more actively corroding surface. The bulk alloy at the same nominal composition as the thin-film displays both a lower $i_{\rm crit}$ and $i_{\rm pass}$ value indicating better passivation. behavior. Fig. 4C compares the LSV of two CL thin-film spots ${\rm Fe_{0.24}Co_{0.30}Ni_{0.27}Cr_{0.10}Al_{0.09}}$ and ${\rm Fe_{0.25}Co_{0.30}Ni_{0.28}Cr_{0.09}Al_{0.08}}$) to both the single composition thin-film and bulk

alloy of the same nominal composition, (FeCoNi) $_{0.84}$ Cr $_{0.10}$ Al $_{0.06}$. These two CL spots are at compositions closest to the (FeCoNi) $_{0.84}$ Cr $_{0.10}$ Al $_{0.06}$ composition of the bulk alloy and single composition thin-film. The data shows that the corrosion potentials of these CL spots are shifted by about + 100 mV with respect to that of the bulk alloy, indicating poorer corrosion resistance. Additionally the separation in current density between $i_{\rm crit}$ and $i_{\rm pass}$ of the CL spots is only about 25 $\mu \rm A/cm^2$ at + 200 mV. The passive current density for the CL spots increases with increasing

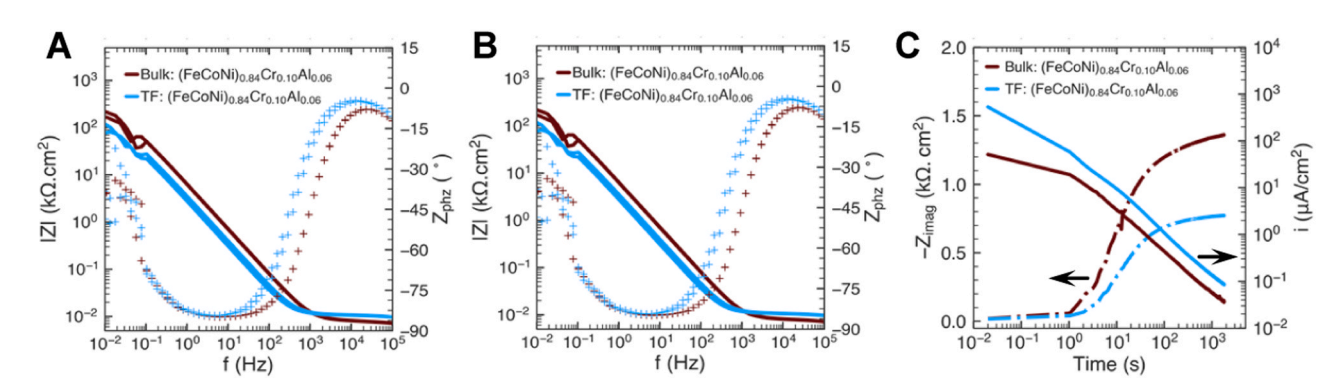


Fig. 5. EIS measurements. Data for the induction-melted bulk and single composition thin-film (FeCoNi) $_{0.84}$ Cr $_{0.10}$ Al $_{0.06}$ alloys. (A) OCP and (B) at + 600 mV SHE after a potentiostatic hold of 1800 s, in deaerated 0.10 mol/L H $_2$ SO $_4$. (C) Current density (dash) and imaginary impedance (dash-dot) transients of bulk and thin-film obtained during the potentiostatic hold at + 600 mV for 1800 s. At OCP, the EIS represents the performance of the air-formed oxide after 1800 s while at + 600 mV represents reduction of the air formed oxide and subsequent passive film formation in the electrolyte.

potential and at + 700 mV it is equal to $i_{\rm crit}$. This behavior of $i_{\rm pass}$ is not observed for either the single composition thin-film or the bulk alloy. We suggest that these differences may result from the larger Al concentrations in the CL wafer spots.

To better understand the differences in the passivation behaviors of bulk vs. thin-film samples, additional electrochemical testing was performed. Fig. 5A shows the comparative results of the single composition (FeCoNi)_{0.84}Cr_{0.10}Al_{0.06} thin-film and induction-melted bulk (FeCo- $\text{Ni})_{0.84}\text{Cr}_{0.10}\text{Al}_{0.06}$ alloy. After 1800 s at OCP, the air-formed oxide of the thin-film showed a lower impedance of 0.15 kΩ·cm², compared to 1.5 $k\Omega$ ·cm² of the bulk alloy at 10 mHz. For the re-passivated film (after cathodic reduction) at +600 mV vs. SHE, the thin-film and bulk samples showed an impedance of 100 k Ω cm² and 200 k Ω ·cm² respectively as shown in Fig. 5B. The solution formed oxides showed a higher impedance compared to the air-formed oxides for both samples while maintaining the same trend of poorer passivation performance metrics for the thin-film. The current density and - Z_{imag} transients shown in Fig. 5C, describe the formation and thickening of the passive film formed in the electrolyte, where - Zimag is a measure of the capacitance and is proportional to oxide thickness [8,41]. At time scales below 1 s both bulk and thin-film alloys show a small $-Z_{imag}$, suggesting minimal coverage of passive film. With time, as the film grows there is an increase in the impedance; the rate of increase is higher for the bulk alloy compared to that of the thin-film. This suggests faster oxide film coverage and growth occurring on the bulk alloy surface. Chronoamperometry at + 600 mV vs. SHE (Fig. 5C) for both the thin-film and bulk sample show exponentially decreasing behavior.

4. Discussion

Both the CL thin-films and the single phase (FeCoNi) $_{0.84}$ Cr $_{0.10}$ Al $_{0.06}$ film contain significant levels of grain boundary porosity that affect passivation behaviors. Fig. 6 shows the typical surface morphology of a FCC single-phase CL spot of composition, (FeCoNi) $_{0.45}$ Cr $_{0.30}$ Al $_{0.25}$, from an earlier set of CL depositions [39]. The total area fraction of grain porosity prior to electrochemical exposure had a mean value of 0.12 ± 0.03 (standard deviation) which did not vary in a statistically relevant manner following passivation.

The surface morphology of the single composition (FeCo-Ni) $_{0.84}$ Cr $_{0.10}$ Al $_{0.06}$ thin-film sample surface was also characterized before electrochemical exposure as shown in Fig. 7A and following passivation, Fig. 7B. Fig. 7A and shows that the thin-film surface contains nanometer-scale grains, which can be seen more clearly in the image inset. After LSV, localized dissolution at the grain boundaries of this sample is observed.

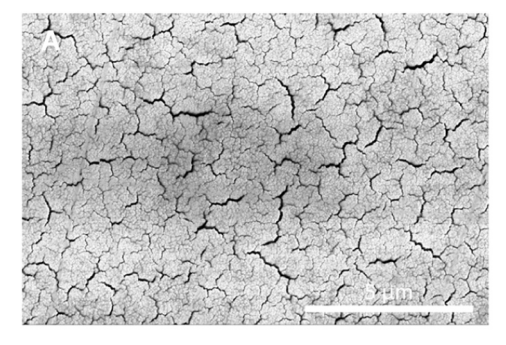
Fig. 8 shows a STEM lift-out taken in order to obtain higher-resolution information about the composition and grain structure of the thin-film sample in cross-section. Fig. 8A is a high-angle annular dark-field (HAADF) image showing that it mostly comprises grains a few

tens of nanometers in size. Fig. 8B shows a STEM-EDS line scan, revealing negligible compositional differences between the grain boundaries and grain interiors. The black line in the line profile shows the grayscale intensity from the image, where the sharp decreases in intensity (marked with arrows) are the location of grain boundaries. The compositional maps in Figs. 8C and 8D are also provided, further highlighting the compositional homogeneity across the film. These data suggest the preferential dissolution observed at the grain boundaries of the thin-film sample is likely caused by intergranular corrosion [42–45]. This behavior is a result of the lower nearest-neighbor coordination of atoms at a grain boundary compared to the grain interior. Different grain facets can corrode and repassivate at different rates depending on their surface orientation [46].

Fig. S4 highlights the dissimilar grain boundary density and grain size between the bulk and single composition (FeCoNi) $_{0.84}$ Cr $_{0.10}$ Al $_{0.06}$ samples. The grain structure of the bulk reveals a columnar-type grain structure resulting from dendritic grain growth during solidification [47, 48]. The linear grain boundary density for the bulk sample was determined to be on average 3 per millimeter (major axis) and 10 per millimeter (minor axis), reflecting the aspect ratio of the columnar grain structure. The grain size of the thin-film sample is in the range of 10–20 nm and the linear grain boundary density is about 60,000 per millimeter.

The CL wafers showed differences in passivation behavior due to the variation in composition and structure across the wafer grid (Fig. 1). The single-phase regions on the CL wafers classified as F, outperformed multi-phase regions FB and FBB2 in this order as shown in Fig. 2. The poor performance in the multi-phase samples can be attributed to the loss of Al and Cr from the FCC matrix to a Cr rich BCC and Al rich (B2 type) intermetallic second phase [25]. This depletes the FCC matrix of Cr in FB alloys and both Cr and Al in FBB2 alloys. The SDC data across these wafer spots shows the passivation performance of the single-phase CL wafer spots improves as the Cr + Al content increases; an expected trend that highlights this method's reliability in predicting alloy compositions that display good passivation behavior. However, MPEA thin-films often include metastable phases and tend towards non-equilibrium structures. In particular, some of these single-phase spots with high Al contents (e.g. Cr_{0.13}Al_{0.19} and Cr_{0.17}Al_{0.13}) would likely contain multiple phases in a bulk alloys synthesized with the same processing conditions used here [49]; the likely B2 secondary phase would lead to a reduction of the overall corrosion performance. The propensity of sputtering to create these non-equilibrium materials is therefore both a drawback and advantage of the thin-film based screening approach: The thin-film properties may not match bulk due to variation in phase composition, but these more exotic phases may elucidate new corrosion behaviors or provide promising new research targets for bulk alloy processing.

Electrochemical metrics of the single-phase CL wafer spots were compared against bulk alloys with similar Cr + Al concentrations and showed qualitatively similar trends with respect to their bulk



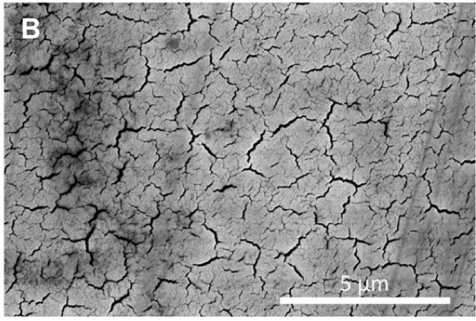


Fig. 6. SEMs of the surface morphology showing grain boundary porosity of the $(FeCoNi)_{0.45}Cr_{0.30}Al_{0.25}$ spot on a CL wafer that has an average grain size of 30 nm. (A) prior to electrochemical exposure and (B) reduction of the air formed film and subsequent passive film formation in the electrolyte at +600 mV SHE. Note that not all the grain boundaries developed porosity.

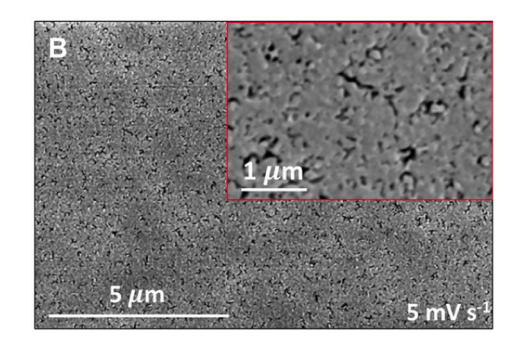


Fig. 7. SEM of the single composition (FeCoNi) $_{0.84}$ Cr $_{0.10}$ Al $_{0.06}$ thin-film surface. (A) before and (B) after LSV at 5 mv/s in 0.10 mol/L H $_2$ SO $_4$. The inset in image B shows considerable grain boundary dissolution.

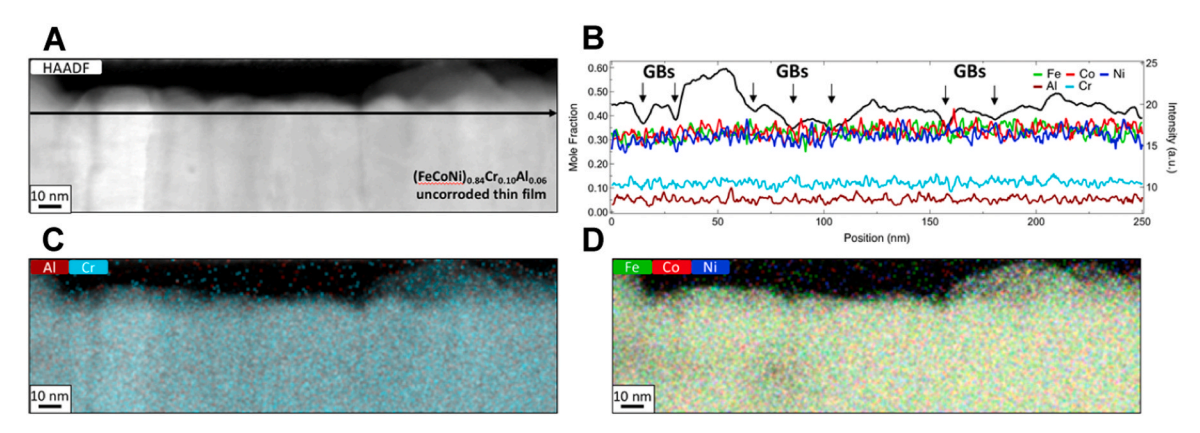


Fig. 8. TEM and STEM-EDS. Data of an uncorroded portion of the single composition (FeCoNi)_{0.84}Cr_{0.10}Al_{0.06} thin-film alloy surface, in cross-section, highlighting the grain structure of the sample and the composition across the grains. (A) HAADF image and (B) STEM-EDS line scan along the black arrow in image A. The colored compositional lines are identified in the plot legend and correspond to the left axis, while the black line is the pixel intensity of the HAADF image (right axis). The grain boundary locations were determined by a decrease in grayscale intensity from the HAADF image. (C) Elemental maps of the (C) Cr and Al and (D) FeCoNi, reveal the compositional homogeneity of the grain interiors and grain boundaries.

counterparts, (Fig. 4.). However, quantitative differences are apparent, as highlighted by the deviations in both the current densities and the voltages identifying the locations i_{crit} and i_{pass} . The (FeCo-Ni) $_{0.84}$ Cr $_{0.10}$ Al $_{0.06}$ thin-film sample, when compared directly to its bulk counterpart, substantiates this finding. These differences are a consequence of the differences in grain boundary porosity, grain size and corresponding grain boundary dissolution of these thin-film and bulk alloy samples. Overall, these data show the of using alloy thin-films and CL wafers to rapidly compare and explore "relative" global electrochemical trends within a wide compositional (and potentially processing) space. However, it is clear that the passivation behavior of thin-film alloys is quantitatively different than bulk alloys of similar composition, indicating the need to validate and benchmark these trends with bulk samples.

5. Conclusions

We investigated a combinatorial library alloy wafer approach, containing 177 alloy spots comprised of a range of different compositions and crystal structures. The structures varied from FCC to FCC+BCC to FCC+BCC+B2 depending on composition. The electrochemical behavior of both single-phase and multi-phase regions was measured across two (FeCoNi)_{1-x-y}Cr_xAl_y CL wafers in a sulfuric acid. These electrochemical behaviors were compared against a set of bulk (FeCoNi)_{1-x-y}Cr_xAl_y (x = 0.04–0.10, y = 0.03 or y = 0.06) alloys and a (FeCoNi)_{0.84}Cr_{0.10}Al_{0.06} alloy thin-film sample following the same protocols. These results demonstrate that significant quantitative differences in passivation metrics exist between bulk and thin-films and that a one-to-one correspondence between thin-film and bulk behavior should not be

expected as a result of the different grain sizes and grain boundary dissolution. However, we found that thin-films of varying composition can be compared relative to one another in terms of common passivation metrics (such as $E_{\rm corr}$, $i_{\rm crit}$, $i_{\rm pass}$, |Z|, etc.) across a CL wafer and that this trend in behavior can be used to predict the likely best bulk sample composition(s) for passivation performance. Importantly, this conclusion is subject to the important caveat that the phase content of the thin-film alloy can be replicated in bulk alloys.

CRediT authorship contribution statement

Howie Joress: Writing - review & editing, Writing - original draft, Validation, Software, Methodology, Investigation, Formal analysis, Data curation. Brian DeCost: Writing - review & editing, Writing - original draft, Software, Methodology, Investigation, Formal analysis, Data curation. Emily F Holcombe: Writing - review & editing, Writing original draft, Investigation. Ben Redemann: Writing - review & editing, Writing - original draft, Methodology, Investigation. Mitra L Taheri: Writing - review & editing, Writing - original draft, Funding acquisition. John R Scully: Writing - review & editing, Writing original draft, Supervision, Methodology, Investigation, Funding acquisition, Conceptualization. Karl Sieradzki: Writing - review & editing, Writing - original draft, Validation, Supervision, Methodology, Investigation, Funding acquisition, Formal analysis, Conceptualization. William H Blades: Writing - review & editing, Writing - original draft, Investigation, Data curation. Debashish Sur: Writing - review & editing, Writing - original draft, Validation, Methodology, Investigation, Data curation. Tyrel M McQueen: Writing – review & editing, Writing – original draft, Supervision, Methodology, Conceptualization. Rohit

Berlia: Writing – review & editing, Writing – original draft, Methodology, Investigation. **Jagannathan Rajagopalan:** Writing – review & editing, Writing – original draft, Supervision, Methodology, Investigation, Funding acquisition.

Author statement

All authors accepted the responsibility for the content of the manuscript, consented to its submission, reviewed all the results, approved the final version of the. manuscript and contributed to its writing and editing.

Declaration of Competing Interest

The authors declare that they have no known competing financial interests or personal relationships that could have appeared to influence the work reported in this paper.

Data availability

Data will be made available on request.

Acknowledgements

The authors gratefully acknowledge partial funding from the Office of Naval Research (ONR) through the Multidisciplinary University Research Initiative (MURI) program, N00014-20-1-2368. The authors also acknowledge the University of Virginia Nanoscale Materials Characterization Facility, the Eyring Materials Center at Arizona State University, and the Johns Hopkins University Materials Characterization and Processing Center. J. Rajagopalan acknowledges support from the National Science Foundation Grant 2223317 (Metals and Metallic Nanostructures program). Use of the Stanford Synchrotron Radiation Lightsource, SLAC National Accelerator Laboratory, is supported by the U.S. Department of Energy, Office of Science, Office of Basic Energy Sciences under Contract no. DE-AC02-76SF00515. Materials processing was performed at the Platform for the Accelerated Realization, Analysis, and Discovery of Interface Materials (PARADIM at JHU), a National Science Foundation Materials Innovation Platform under Grant no. NSF DMR-2039380. The authors thank J. Hattrick-Simpers (University of Toronto) for his assistance in carrying out these experiments and A Mehta (SLAC), N Johnson (SLAC), and N Patra (SLAC) for collecting the synchrotron diffraction data.

Appendix A. Supporting information

Supplementary data associated with this article can be found in the online version at doi:10.1016/j.corsci.2024.112261.

References

- B. Cantor, I.T.H. Chang, P. Knight, A.J.B. Vincent, Microstructural development in equiatomic multicomponent alloys. Mater. Sci. Eng. A 375-377 (2004) 213–218.
- [2] B. Gludovatz, A. Hohenwarter, D. Catoor, E.H. Chang, E.P. George, R.O. Ritchie, A fracture-resistant high-entropy alloy for cryogenic applications, Science 345 (2014) 1153–1158.
- [3] Z. Li, S. Zhao, R.O. Ritchie, M.A. Meyers, Mechanical properties of high entropy alloys with emphasis on face-centered cubic alloys, Prog. Mater. Sci. 102 (2019) 296–345.
- [4] Y. Shi, B. Yang, P.K. Liaw, Corrosion-resistant high-entropy alloys: a review, Metals 7 (2017) 43.
- [5] N. Birbilis, S. Choudhary, J.R. Scully, M.L. Taheri, A perspective on corrosion of multi-principal element alloys, npj Mater. Degrad.. 5 (2021) 1–8.
- [6] T.M. Butler, M.L. Weaver, Oxidation behavior of arc melted AlCoCrFeNi multicomponent high-entropy alloys, J. Alloy. Compd. 674 (2016) 229–244.
- [7] D.B. Miracle, O.N. Senkov, A critical review of high entropy alloys and related concepts, Acta Mater. 122 (2017) 448–511.
- [8] S. Choudhary, D.D. Thomas, Macdonald, N. Birbilis, Growth kinetics of multi-oxide passive film formed upon the multi-principal element alloy AlTiVCr: effect of transpassive dissolution of V and Cr, J. Electrochem. Soc. 168 (2021) 051506.

[9] Y. Shi, B. Yang, X. Xie, J. Brechtl, K.A. Dahmen, P.K. Liaw, Corrosion of AlxCoCrFeNi high-entropy alloys: Al-content and potential scan-rate dependent pitting behavior, Corros. Sci. 119 (2017) 33–45.

- [10] Y. Shi, L. Collins, N. Balke, P.K. Liaw, B. Yang, In-situ electrochemical-AFM study of localized corrosion of AlxCoCrFeNi high-entropy alloys in chloride solution, Appl. Surf. Sci. 439 (2018) 533–544.
- [11] F. Ye, Z. Jiao, S. Yan, L. Guo, L. Feng, J. Yu, Microbeam plasma arc remanufacturing: effects of Al on microstructure, wear resistance, corrosion resistance and high temperature oxidation resistance of AlxCoCrFeMnNi highentropy alloy cladding layer, Vacuum 174 (2020) 109178.
- [12] M. Li, Q. Zhang, B. Han, L. Song, J. Li, J. Yang, Investigation on microstructure and properties of AlxCoCrFeMnNi high entropy alloys by ultrasonic impact treatment, J. Alloy. Compd. 816 (2020) 152626.
- [13] M. Izadi, M. Soltanieh, S. Alamolhoda, S.M.S. Aghamiri, M. Mehdizade, Microstructural characterization and corrosion behavior of AlxCoCrFeNi high entropy alloys, Mater. Chem. Phys. 273 (2021) 124937.
- [14] S. Choudhary, S. O'Brien, Y. Qiu, S. Thomas, R.K. Gupta, N. Birbilis, On the dynamic passivity and corrosion resistance of a low cost and low-density multiprincipal-element alloy produced via commodity metals, Electrochem. Commun. 125 (2021) 106989.
- [15] S. Inman, D. Sur, J. Han, K.M. Ogle, J.R. Scully, Corrosion behavior of a compositionally complex alloy utilizing simultaneous Al, Cr, and Ti passivation, Corros. Sci. 217 (2023) 111–138.
- [16] Y. Xie, D.M. Artymowicz, P.P. Lopes, A. Aiello, D. Wang, J.L. Hart, E. Anber, M. L. Taheri, H. Zhuang, R.C. Newman, K. Sieradzki, A percolation theory for designing corrosion-resistant alloys, Nat. Mater. 20 (2021) 789–793.
- [17] W.-C. Chiang, W.-C. Luu, J. Wu, Effect of aluminum content on the passivation behavior of Fe-Al alloys in sulfuric acid solution, J. Mater. Sci. 41 (2006) 3041–3044.
- [18] J. Peng, F. Moszner, J. Rechmann, D. Vogel, M. Palm, M. Rohwerder, Influence of Al content and pre-oxidation on the aqueous corrosion resistance of binary Fe-Al alloys in sulphuric acid, Corros. Sci. 149 (2019) 123–132.
- [19] H. Springer, C. Baron, L. Tanure, M. Rohwerder, A combinatorial study of the effect of Al and Cr additions on the mechanical, physical and corrosion properties of Fe, Mater. Today Commun., vol. 29, 2021, 102947.
- [20] Q. Bai, K. Sieradzki, Why do Fe–Al alloys show good passivation behavior in acids compared to elemental Al? J. Electrochem. Soc. 170 (2023) 021510.
- [21] R.P. Frankenthal, On the passivity of iron-chromium alloys III. Effect of potential, J. Electrochem. Soc. 116 (1969) 1646–1651.
- [22] W. Chai, T. Lu, Y. Pan, Corrosion behaviors of FeCoNiCrx (x = 0, 0.5, 1.0) multiprincipal element alloys: role of Cr-induced segregation, Intermetallics 116 (2019) 106654.
- [23] S.B. Inman, J. Han, A.Y. Gerard, J. Qi, M.A. Wischhusen, S.R. Agnew, S.J. Poon, K. Ogle, J.R. Scully, Effect of Mn content on the passivation and corrosion of Al0.3Cr0.5Fe2MnxMo0.15Ni1.5Ti0.3 compositionally complex face-centered cubic alloys. Corrosion 78 (2022) 32–48.
- [24] H. Luo, Z. Li, A.M. Mingers, D. Raabe, Corrosion behavior of an equiatomic CoCrFeMnNi high-entropy alloy compared with 304 stainless steel in sulfuric acid solution, Corros. Sci. 134 (2018) 131–139.
- [25] E.A. Anber, A.C. Lang, E.A. Lass, P.K. Suri, J.L. Hart, D.S. D'Antuono, H. Diao, R. Feng, R. Doherty, P.K. Liaw, M.L. Taheri, Insight into the kinetic stabilization of Al0.3CoCrFeNi high-entropy alloys, Materialia 14 (2020) 100872.
- [26] C.C. Yen, H.N. Lu, M.H. Tsai, B.W. Wu, Y.C. Lo, C.C. Wang, S. Chang, S.K. Yen, Corrosion mechanism of annealed equiatomic AlCoCrFeNi tri-phase high-entropy alloy in 0.5 M H2SO4 aerated aqueous solution, Corros. Sci. 157 (2019) 462–471.
- [27] C.P. Lee, C.C. Chang, Y.Y. Chen, J.W. Yeh, H.C. Shih, Effect of the aluminium content of AlxCrFe1.5MnNi0.5 high-entropy alloys on the corrosion behaviour in aqueous environments, Corros. Sci. 50 (2008) 2053–2060.
- [28] C. Ren, L. Ma, D. Zhang, X. Li, A. Mol, High-throughput experimental techniques for corrosion research: a review, MGE Adv. 1 (2023) e20.
- [29] C. Ren, L. Ma, X. Luo, C. Dong, T. Gui, B. Wang, X. Li, D. Zhang, High-throughput assessment of corrosion inhibitor mixtures on carbon steel via droplet microarray, Corros. Sci. 213 (2023) 110967.
- [30] T.H. Muster, A.E. Hughes, S.A. Furman, T. Harvey, N. Sherman, S. Hardin, P. Corrigan, D. Lau, F.H. Scholes, P.A. White, M. Glenn, J. Mardel, S.J. Garcia, J.M. C. Mol, A rapid screening multi-electrode method for the evaluation of corrosion inhibitors, Electrochim. Acta 54 (2009) 3402–3411.
- [31] C. Gao, B. Hu, I. Takeuchi, K-S, X.-D. Xiang, G. Wang, Quantitative scanning evanescent microwave microscopy and its applications in characterization of functional materials libraries, Meas. Sci. Technol. 16 (2005) 248–260.
- [32] A.I. Mardare, A.P. Yadav, A.D. Wieck, M. Stratmann, A.W. Hassel, Combinatorial electrochemistry on Al-Fe alloys, Sci. Technol. Adv. Mater. 9 (2008) 035009.
- [33] A.I. Mardare, A. savan, A. Ludwig, A.D. Wieck, A.W. Hassel, A combinatorial passivation study of Ta–Ti alloys, Corros. Sci. 51 (2009) 1519–1527.
- [34] J. Nie, L. Wei, D.-l Li, L. Zhao, Y. Jiang, Q. Li, High-throughput characterization of microstructure and corrosion behavior of additively manufactured SS316L-SS431 graded material, Addit. Manuf. 35 (2020) 101295.
- [35] A.W. Hassel, M.M. Lohrengel, The scanning droplet cell and its application to structured nanometer oxide films on aluminum, Electrochim. Acta 42 (1997) 3327–3333.
- [36] K.A. Lill, A.W. Hassel, G. Frommeyer, M. Stratmann, Scanning droplet cell investigations on single grains of a FeAlCr light weight ferritic steel, Electrochim. Acta 51 (2005) 978–983.
- [37] H. Joress, B. DeCost, N. Hassan, T.M. Braun, J.M. Gorham, J. HattrickSimpers, Development of an automated millifluidic platform and data-analysis pipeline for

- rapid electrochemical corrosion measurements: a pH study on Zn-Ni, Electrochim. Acta 428 (2022) 140866.
- [38] J.R. Hattrick-Simpers, B. DeCost, A.G. Kusne, H. Joress, W. Wong-Ng, D.L. Kaiser, A. Zakutayev, C. Phillips, S. Sun, J. Thapa, H. Yu, I. Takeuchi, T. Buonassisi, An open combinatorial diffraction dataset including consensus human and machine learning labels with quantified uncertainty for training new machine learning models, Integr. Mater. Manuf. Innov. 10 (2021) 311–318.
- [39] D. Sur, E.F. Holcombe, W.H. Blades, E.A. Anber, D.L. Foley, B.L. DeCost, J. Liu, J. Hattrick-Simpers, K. Sieradzki, H. Joress, J.R. Scully, M.L. Taheri, An experimental high-throughput to high-fidelity study towards discovering Al–Cr containing corrosion-resistant compositionally complex alloys, High Entropy Alloy. Mater. 1 (2023) 336–353.
- [40] J.R. Scully, Polarization resistance method for determination of instantaneous corrosion rates, Corrosion 56 (2000) 199–217.
- [41] K.L. Cwalina, H.M. Ha, N. Ott, P. Reinke, N. Birbilis, J.R. Scully, In operando analysis of passive film growth on Ni-Cr and Ni-Cr-Mo alloys in chloride solutions, J. Electrochem. Soc. 166 (2019) C3241–C3253.
- [42] D. An, T.A. Griffiths, P. Konijnenberg, S. Mandal, Z. Wang, S. Zaefferer, Correlating the five-parameter grain boundary character distribution and the intergranular corrosion behaviour of a stainless steel using 3d orientation microscopy based on mechanical polishing serial sectioning, Acta Mater. 156 (2018) 297–309.

- [43] N. Badwe, X. Chen, D.K. Schreiber, M.J. Olszta, N.R. Overman, E.K. Karasz, A. Y. Tse, S.M. Bruemmer, K. Sieradzki, Decoupling the role of stress and corrosion in the intergranular cracking of noble-metal alloys, Nat. Mater. 17 (2018) 887–893.
- [44] E. Martinez-Lombardia, L. Lapeire, V. Maurice, I. De Graeve, K. Verbeken, L. H. Klein, L.A.I. Kestens, P. Marcus, H. Terryn, In situ scanning tunneling microscopy study of the intergranular corrosion of copper, Electrochem. Commun. 41 (2014) 1–4.
- [45] M. Bettayeb, V. Maurice, L.H. Klein, L. Lapeire, K. Verbeken, P. Marcus, Nanoscale intergranular corrosion and relation with grain boundary character as studied in situ on copper, J. Electrochem. Soc. 165 (11) (2018) C835–C841.
- [46] K. Gusieva, K.L. Cwalina, W.H. Blades, G. Ramalingam, J.H. Perepezko, P. Reinke, J.R. Scully, Repassivation behavior of individual grain facets on dilute Ni-Cr and Ni-Cr-Mo alloys in acidified chloride solution, J. Phys. Chem. C 122 (2018) 19499–19513.
- [47] W. Kurz, C. Bezencon, M. Gaumann, Columnar to equiaxed transition in solidification processing, Sci. Technol. Adv. Mater. 2 (2001) 185–191.
- [48] J.A. Spittle, Columnar to equiaxed grain transition in as solidified alloys, Int. Mater. Rev. 51 (2006) 247–269.
- [49] W.H. Blades, B.W.Y. Redemann, N. Smith, D. Sur, M.S. Barbieri, Y. Xie, S. Lech, E. Anber, M.L. Taheri, C. Wolverton, T.M. McQueen, J.R. Scully, K. Sieradzki, Tuning chemical short-range order for stainless behavior at reduced chromium concentrations in multi-principal element alloys, arXiv preprint, arXiv id: 2403.00086, 2024.